ARTICLES
https://doi.org/10.1038/s41566-018-0175-7

nature photonics

Gate-tunable third-order nonlinear optical response of massless Dirac fermions in graphene

Tao Jiang[1,9], Di Huang[1,9], Jinluo Cheng[2], Xiaodong Fan[3,4], Zhihong Zhang[5], Yuwei Shan[1], Yangfan Yi[1], Yunyun Dai[1], Lei Shi[1,6], Kaihui Liu[5], Changgan Zeng[3,4], Jian Zi[1,6], J. E. Sipe[7], Yuen-Ron Shen[1,8], Wei-Tao Liu[1,6]* and Shiwei Wu[1,6]*

Graphene with massless Dirac fermions can have exceptionally strong third-order optical nonlinearities. Yet reported values of nonlinear optical susceptibilities for third-harmonic generation (THG), four-wave mixing (FWM) and self-phase modulation vary over six orders of magnitude. Such variation likely arises from frequency-dependent resonance effects of different processes in graphene under different doping. Here, we report an experimental study of THG and FWM in graphene using gate tuning to adjust the doping level and vary the resonant condition. We find that THG and sum-frequency FWM are strongly enhanced in heavily doped graphene, while the difference-frequency FWM appears just the opposite. Difference-frequency FWM exhibited a novel divergence towards the degenerate case in undoped graphene, leading to a giant enhancement of the nonlinearity. The results are well supported by theory. Our full understanding of the diverse nonlinearity of graphene paves the way towards future design of graphene-based nonlinear optoelectronic devices.

Graphene exhibits extraordinarily strong coupling to light owing to its unique linear and gapless two-dimensional band structure that hosts massless Dirac fermions[1,2]. The wide band linearity results in a unique spectral response ranging from terahertz and infrared to visible and ultraviolet. The corresponding optical absorbance is a constant universal value of 2.3% for a suspended graphene monolayer[3,4]. Gate tuning of the carrier density, and hence the chemical potential (or Fermi level), modifies both intraband and interband transitions in graphene, and allows control of its optical properties in selected spectral regimes, leading to many promising applications in optoelectronics and photonics[1,2,5–9].

The very strong linear response in such regimes suggests that the nonlinear optical response of graphene could also be exceptionally strong and promising for optoelectronic applications[10,11]. As second-order nonlinearity in graphene is electric-dipole forbidden because of inversion symmetry, the third-order nonlinear optical response becomes dominant. Indeed, third-harmonic generation (THG)[12–15], four-wave mixing (FWM)[16,17], optical Kerr effect[18–21], self-phase modulation[22,23], two-colour coherent optical injection of current[24] and even high-harmonic generations[25] can be readily observed in graphene. However, the reported values of the third-order nonlinear susceptibilities appear to vary by more than six orders of magnitude (see Supplementary Table 1). It is not yet clear how such a wide variation comes about despite differences between the nonlinear processes studied and the experimental conditions employed. A unified understanding of the nonlinear optical response of graphene is needed, and is crucial for future design of graphene-based nonlinear photonic devices[6,22]. It will also provide a salient platform for study of the third-order nonlinear optical response of massless Dirac fermions that exist in other novel materials such as topological insulators[26] and Dirac and Weyl semimetals[27].

For a better understanding of the third-order optical response of graphene, we must know how it varies with input frequencies with respect to the chemical potential. Tuning the input frequencies or the chemical potential can move a third-order nonlinear process in and out of one-, two- or three-photon resonances, and provide detailed information about the nonlinear process. Unfortunately, such experiments have not yet been reported, although they have been suggested in theoretical work[28–32].

Here, we report an experimental study of the third-order nonlinear optical response of ion-gel-gated graphene. Our focus is on THG and FWM, but the extension to other third-order processes is straightforward. The ion-gel gating allowed us to controllably tune the chemical potential over a sufficiently large range such that one-, two- and three-photon resonances could be selectively turned on or off for a given set of input frequencies. We found that THG and sum-frequency FWM in the heavily doped graphene could be much stronger (~30 times) than in undoped graphene, while difference-frequency FWM behaved just the opposite, and exhibited a strong divergence of nonlinearity towards the degenerate FWM in undoped graphene. Our experimental results matched well with the theoretical calculation following refs [28,29]. Thus, this study provides a firm basis for comprehension of third-order nonlinear optical processes in graphene and graphene-like Dirac materials.

---

[1]State Key Laboratory of Surface Physics, Key Laboratory of Micro and Nano Photonic Structures (MOE), Department of Physics, and Institute for Nanoelectronic Devices and Quantum Computing, Fudan University, Shanghai, China. [2]Changchun Institute of Optics, Fine Mechanics and Physics, Chinese Academy of Sciences, Changchun, Jilin, China. [3]International Center for Quantum Design of Functional Materials, Hefei National Laboratory for Physical Sciences at the Microscale, and Synergetic Innovation Center of Quantum Information and Quantum Physics, University of Science and Technology of China, Hefei, China. [4]CAS Key Laboratory of Strongly-Coupled Quantum Matter Physics, and Department of Physics, University of Science and Technology of China, Hefei, China. [5]State Key Laboratory for Mesoscopic Physics and School of Physics, Peking University, Beijing, China. [6]Collaborative Innovation Center of Advanced Microstructures, Nanjing, China. [7]Department of Physics, University of Toronto, Toronto, Ontario, Canada. [8]Physics Department, University of California, Berkeley, CA, USA. [9]These authors contributed equally: Tao Jiang, Di Huang. *e-mail: wtliu@fudan.edu.cn; swwu@fudan.edu.cn

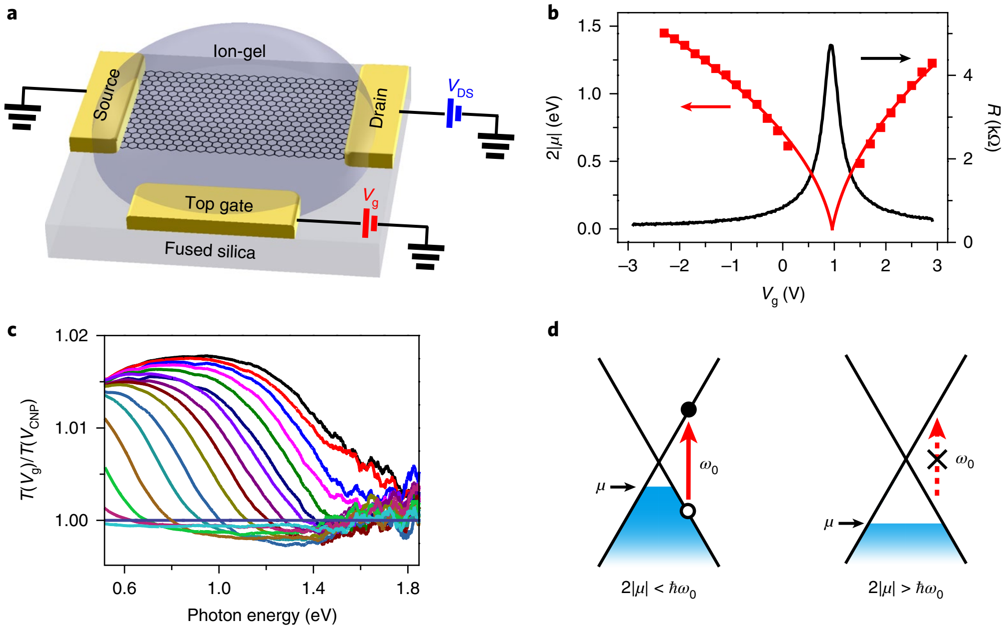

Fig. 1 | Tuning of chemical potential in graphene by ion-gel gating. a, Schematic of an ion-gel-gated graphene monolayer on a fused silica substrate covered by ion-gel and voltage biased by the top gate. The source and drain electrodes on graphene with voltage V_{DS} applied are for resistance measurement. **b**, Measured graphene resistance (R) as a function of gate voltage V_g (black curve), the peak of which refers to the CNP or zero chemical potential ($\mu = 0$). The red squares and curve are $2|\mu|$ versus V_g deduced from the transmittance spectra in **c** and calculated for the graphene device with a fitted ion-gel capacitance of 2.5 μF cm^{-2} (discussed in the Supplementary Information), respectively. **c**, Transmittance spectra of graphene gated at different $V_g - V_{CNP}$, normalized against the one gated at V_{CNP}. Spectra from left to right correspond to $V_g - V_{CNP}$ changed from 0 to −3.2 V in steps of 0.2 V. The transmittance increases when $2|\mu| > \hbar\omega_0$. **d**, Linearly dispersed electronic bands of graphene around the CNP showing that tuning of μ enables Pauli blocking of interband transitions when $2|\mu| > \hbar\omega_0$.

Shift of chemical potential by gate tuning

For gate tuning of the chemical potential, we adopted the ion-gel gating method using the field-effect transistor structure with graphene supported by fused silica[9,33,34], as depicted in Fig. 1a. This device structure enabled us to measure the linear and nonlinear optical responses of graphene at room temperature and monitor in situ the chemical potential μ versus the gate voltage V_g. Figure 1b plots the graphene resistance as a function of V_g. At $V_g \approx 0.9$ V, the resistance is maximum, indicating that graphene is at the charge neutral point (CNP, $\mu = 0$). Away from the CNP, the resistance decreases and μ shifts to positive or negative values accordingly.

To extract the chemical potential μ as a function of V_g, we measured the transmittance spectra of the gated sample at normal incidence[35]. The spectra at different V_g normalized against the one at V_{CNP} are shown in Fig. 1c. As described in Fig. 1d, the interband transitions should be suppressed by Pauli blocking for photon energy $\hbar\omega_0 < 2|\mu|$, where ω_0 is the angular frequency of light, resulting in a step-like transmission spectrum if the temperature and damping effects are neglected. At finite temperature and with proper damping factors, the spectrum is broadened into a shoulder-like one, as seen in Fig. 1c. We could use the Kubo formula to fit each spectrum and deduce $|\mu|$ from the fitting (described in the Supplementary Information)[35]. The deduced $|\mu|$ as a function of V_g is plotted in Fig. 1b. The result agrees well with that (red curve in Fig. 1b) predicted from an ion-gel-gated graphene device with a capacitance of 2.5 μF cm^{-2} (see the Supplementary Information). The uncertainty of $|\mu|$ so obtained was ±10 meV. Ion-gel gating permitted us to tune $|\mu|$ from 0 to ~0.9 eV (ref. [9]), corresponding to a tuning of the carrier density of graphene from 0 to ~6×10^{13} cm^{-2}.

Experiment on THG

The linearly polarized femtosecond laser at 1,566 nm ($\hbar\omega_0 = 0.794$ eV) was used to excite THG of ion-gel-gated graphene at normal incidence, as described in the Methods. Two representative output spectra taken in the reflected direction at $\mu = 0$ and $\mu = -0.74$ eV are shown in Fig. 2a. The former shows a THG peak at 2.381 eV superimposed on a broad background, which is absent in the latter. The broad background is known to be due to ultrafast photoluminescence arising from Auger-like scattering of one-photon excited carriers[36]. It disappears when $2|\mu|$ is larger than $\hbar\omega_0$ so that the one-photon excitation is Pauli blocked. While the THG peak was readily observable at all μ (Fig. 2b), its intensity exhibits shoulder-like rises as $2|\mu|$ moves over $\hbar\omega_0$ and $2\hbar\omega_0$ and reaches a maximum strength of ~30 times that of $\mu = 0$, as seen from the curves plotted in Fig. 2c for four different input wavelengths: 1,300 nm (0.956 eV), 1,400 nm (0.888 eV), 1,566 nm (0.794 eV) and 1,650 nm (0.753 eV). As will be explained more clearly later, these shoulder-like features arise from stepwise switching off of resonant transitions in graphene when $|\mu|$ increases: one-photon, two-photon and three-photon resonant transitions are switched off successively when $2|\mu|$ becomes larger than $\hbar\omega_0$, $2\hbar\omega_0$ and $3\hbar\omega_0$ (unfortunately, the last step could not be reached in our experiment). Note that without graphene on the substrate, THG from the ion-gel-gated fused silica was not observable.

The dependence of THG on input/output polarization is governed by the D_{6h} structural symmetry of graphene. We found that if the normally incident input was linearly polarized and the analyser for the reflected THG was set at an angle θ with respect to the input polarization, the observed THG output was proportional to $\cos^2\theta$. Figure 2d presents two examples of THG versus θ taken at $\mu = -0.89$ eV with input polarizations along and perpendicular to the source–drain direction (Fig. 1a), respectively. In another measurement, we set the output analyser parallel to the input polarization and rotated them together with respect to the sample about its surface normal. The observed THG was isotropic, independent of the azimuthal rotation (Fig. 2e). Both results can be understood knowing that the third-order nonlinear susceptibility element,

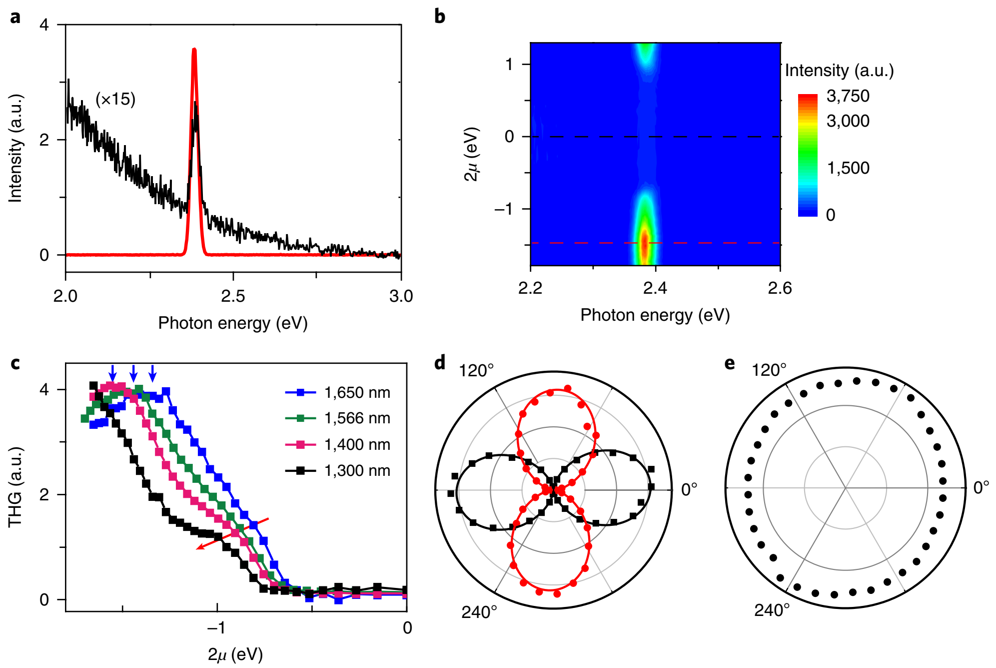

Fig. 2 | Gate-controlled THG from graphene and its polarization patterns. **a**, Measured THG spectra by a normally incident femtosecond input pulse at 1,566 nm from graphene gated at $\mu = 0$ (black curve, magnified by 15 times) and $\mu = -0.74$ eV (red curve). The broadband background of the black curve comes from up-converted photoluminescence due to rapid carrier–carrier scattering following one-photon interband excitation. **b**, Measured spectra versus 2μ and photon energy showing strong dependence of THG at 2.381 eV with μ. The spectra in **a** correspond to the signal variation following the black and red dashed lines. **c**, THG signal as a function of 2μ generated by different input wavelengths: 1,300 nm, 1,400 nm, 1,566 nm and 1,650 nm. The corresponding incident laser fluences were 3.14, 3.68, 2.86 and 1.54 J m^{-2}, respectively. Curves are normalized for comparison. Dots are experimental data and curves are guides for the eye. Red and blue arrows mark the shoulder and maximum regions, respectively. **d**,**e**, Illustration that a linearly polarized input generates a linearly co-polarized THG output (with $\mu = -0.89$ eV). In **d**, THG output through an analyser is plotted as a function of angle θ between the analyser axis and the input polarization set along (black) and perpendicular to (red) the source–drain directions. In both cases, the experimental data (dots) can be well fit by a $\cos^2\theta$ curve. In **e**, with the analyser axis parallel to the input polarization and rotating together azimuthally with respect to the sample, the THG output appears isotropic.

$\chi^{(3)}_{xxxx}$, of graphene is responsible for the THG (see the Supplementary Information).

Experiment on FWM

FWM with two input frequencies ω_1 and ω_2 ($\omega_1 > \omega_2$) is a more general process than THG, but the effect of shifting μ to switch resonant transitions on and off is similar. Four FWM processes, described in Fig. 3a, are considered here: two sum-frequency mixings (SFM) with output at $2\omega_1 + \omega_2$ and $\omega_1 + 2\omega_2$, and two difference-frequency mixings (DFM) with output at $2\omega_1 - \omega_2$ and $2\omega_2 - \omega_1$. In our experiment, we chose $\hbar\omega_1 = 1.195$ eV (1,040 nm) and $\hbar\omega_2 = 0.956$ eV (1,300 nm), which generated SFM outputs at 3.346 eV (371 nm) and 3.107 eV (400 nm), and DFM outputs at 1.434 eV (867 nm) and 0.717 eV (1,734 nm). The last DFM output was outside our spectral detection range. To study this process, we slightly shifted $\hbar\omega_2$ to 0.994 eV (1,250 nm) to generate DFM ($2\omega_2 - \omega_1$) at 0.794 eV (1,566 nm). The observed spectra taken at $\mu = 0$ and $\mu = -0.73$ eV for the four mixing processes are displayed in Fig. 3b–d, showing the respective spectral peaks.

The SFM peaks are much stronger at $|\mu| = 0.73$ eV than at $\mu = 0$, but the DFM peaks show the opposite trend. The SFM processes are expected to be quite similar to THG, exhibiting a shoulder-like rise as $2|\mu|$ approaches $\hbar\omega_1$ and $\hbar\omega_2$ (individual shoulders merge into one because of broadening). This is seen for the $\hbar(\omega_1 + 2\omega_2)$ process in Fig. 3e. The curve shows another rise as $2|\mu|$ approaches $2\hbar\omega_1$, $2\hbar\omega_2$ and $\hbar(\omega_1 + \omega_2)$. Unfortunately, the top of the rise cannot be seen because it was outside the tuning range of $|\mu|$. The DFM processes behave oppositely: at $\mu = 0$, the output is strong, but as $2|\mu|$ moves towards $\hbar\omega_1$, $\hbar\omega_2$, $\hbar(2\omega_1 - \omega_2)$ or $\hbar(2\omega_2 - \omega_1)$, it shows a step-like drop, as seen in Fig. 3e for the $2\omega_1 - \omega_2$ process and Fig. 3f for both DFM processes.

Theoretical understanding and comparison with experiment

To understand the observed μ-dependences of THG and FWM in graphene in depth, we resort to the theory developed by Cheng et al.[28,29]. The analytical expression of the third-order nonlinear susceptibility, $\chi^{(3)}$, generally has 8 terms for THG and 24 terms for the FWM processes studied here[37,38]. In our case, $\chi^{(3)}$ of graphene is dominated by contributions from interband transitions; with the gapless, linearly dispersed band structure, each term in $\chi^{(3)}$ can only have a single resonance at either $\omega_i = 2v_F|k|$ or $|\omega_i \pm \omega_j| = 2v_F|k|$ or $|2\omega_i \pm \omega_j| = 2v_F|k|$ that provides the resonant enhancement. Here, ω_i and ω_j refer to the input frequencies, which can be either ω_1 or ω_2 in practice, v_F is the Fermi velocity in graphene and k is the electron wavevector in the first Brillouin zone. The abovementioned resonances can be switched off by Pauli blocking if $2|\mu|$ becomes larger than $\hbar\omega_i$, $|\hbar\omega_i \pm \hbar\omega_j|$ and $|2\hbar\omega_i \pm \hbar\omega_j|$, respectively. It is expected that switch-off of resonances will introduce characteristic changes of $\chi^{(3)}$.

Mathematically, we can write a single resonant term in $\chi^{(3)}$ in the form of $\int \frac{A(k)\Delta n(k,\mu)}{\omega_I - 2v_F|k|} d^2k$, where $A(k)$ is the product of transition matrix elements and off-resonance denominators, ω_I is the input frequency or frequency combination on interband resonant transition and $\Delta n(k, \mu)$ is the difference of Fermi distributions of electrons between valence and conduction bands. The dependence

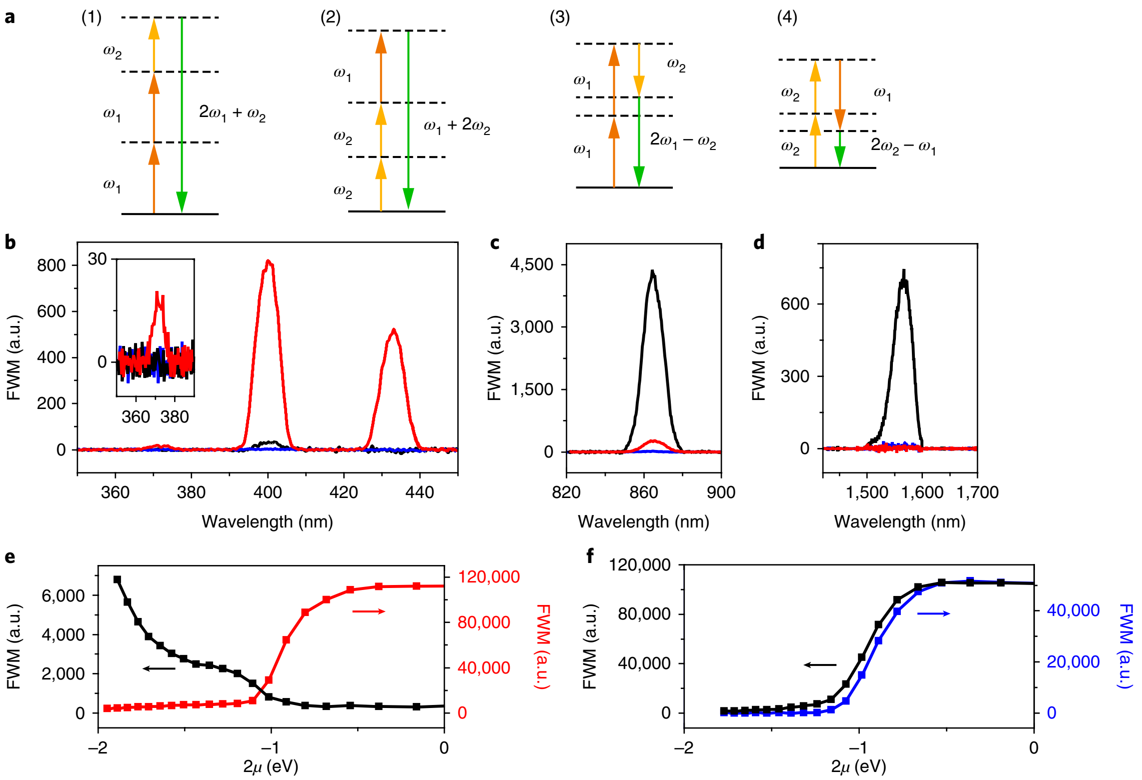

Fig. 3 | FWM in gated graphene. a, FWM processes (1)–(4) by two-colour excitation of ω_1 and ω_2 ($\omega_1 > \omega_2$). Processes (1) and (2) depict SFM of $2\omega_1 + \omega_2$ and $\omega_1 + 2\omega_2$, respectively. Processes (3) and (4) depict DFM of $2\omega_1 - \omega_2$ and $2\omega_2 - \omega_1$, respectively. **b**–**d**, Output spectra of THG and SFM with output at $3\omega_2$ at 433 nm, $\omega_1 + 2\omega_2$ at 400 nm, $2\omega_1 + \omega_2$ at 371 nm (**b**), DFM with output at $2\omega_1 - \omega_2$ at 867 nm (**c**) and DFM with output at $2\omega_2 - \omega_1$ at 1,566 nm (**d**). The input wavelengths and laser fluences were 1,040 nm, 0.58 J m^{-2} at ω_1 and 1,300 nm, 0.72 J m^{-2} at ω_2 for **b** and for the data points in black in **e**; 1,040 nm, 0.74 J m^{-2} at ω_1 and 1,300 nm, 1.1 J m^{-2} at ω_2 for **c** and for the data points in red in **e**; 1,040 nm, 0.64 J m^{-2} at ω_1 and 1,250 nm, 1.16 J m^{-2} at ω_2 for **d** and **f**, respectively. Black and red spectra are for $\mu = 0$ and $\mu = -0.73$ eV, respectively. Blue spectra from the silica substrate are presented as reference. The inset in **b** shows the SFM signal at 371 nm, which is weak because of the limited sensitivity of our detector. **e**, Outputs of SFM at $\omega_1 + 2\omega_2$ (black) and DFM at $2\omega_1 - \omega_2$ (red) as functions of 2μ. Dots are experimental data and curves are guides for the eye. **f**, Outputs of DFM at $2\omega_1 - \omega_2$ (black) and DFM at $2\omega_2 - \omega_1$ (blue) as functions of 2μ.

of $\chi^{(3)}$ on μ is through $\Delta n(k, \mu)$, which has a derivative $\partial \Delta n(k, \mu) / \partial \mu \sim \delta(|\mu| - v_F|k|)$ at $T \sim 0$ K. We then have $\partial \chi^{(3)}(\mu) / \partial \mu \propto \frac{1}{2\mu - \hbar\omega_I}$. As $\frac{1}{2\mu - \hbar\omega_I} = \mathcal{P}\frac{1}{2\mu - \hbar\omega_I} + i\pi\delta(2\mu - \hbar\omega_I)$ for $2\mu \sim \hbar\omega_I$, with $\mathcal{P}$ and δ denoting the principal value and delta function, respectively, we find $\chi^{(3)} \propto [\ln|2\mu - \hbar\omega_I| + i\pi H(2\mu - \hbar\omega_I)]$ as 2μ moves across $\hbar\omega_I$, where $H(2\mu - \hbar\omega_I)$ is the Heaviside step function, equal to 0 for $2|\mu| < \hbar\omega_I$ and 1 for $2|\mu| > \hbar\omega_I$, and $\ln|2\mu - \hbar\omega_I|$ exhibits a divergent peak at $|2\mu| = |\hbar\omega_I|$. The full mathematical derivation of $\chi^{(3)}$ for graphene, including contributions from both interband and intraband transitions, has been worked out by Cheng et al.[28], which is sketched in the Supplementary Information. We have carried out calculation following their theory to compare with our experimental results.

Consider THG first, which is the simplest among all third-order processes. The analytic expression of Cheng et al. has a concise form $\chi^{(3)}_{xxxx} \propto \left[-17G\left(\frac{\hbar\omega_0}{2|\mu|}\right) + 64G\left(\frac{2\hbar\omega_0}{2|\mu|}\right) - 45G\left(\frac{3\hbar\omega_0}{2|\mu|}\right)\right]$ with $G(x) = \ln\left|\frac{1+x}{1-x}\right| + i\pi H(|x| - 1)$. The three G terms in the brackets describe switching off of one-, two- and three-photon resonant transitions as $2|\mu|$ moves over $\hbar\omega_0$, $2\hbar\omega_0$ and $3\hbar\omega_0$, as illustrated in Fig. 4a. Note that the signs of the first and third terms for one-photon and three-photon resonant transitions are opposite to that of the second term for two-photon resonant transition. When $2|\mu| < \hbar\omega_0$, all three terms contribute to $\chi^{(3)}_{xxxx}$, but they nearly cancel each other, leaving $\chi^{(3)}_{xxxx}$ very small. With $\hbar\omega_0 < 2|\mu| < 2\hbar\omega_0$, one-photon resonant transition is blocked and $G\left(\frac{\hbar\omega_0}{2|\mu|}\right) \sim 0$; imperfect cancellation of the $G\left(\frac{2\hbar\omega_0}{2|\mu|}\right)$ and $G\left(\frac{3\hbar\omega_0}{2|\mu|}\right)$ terms leads to a significant positive value of $\chi^{(3)}_{xxxx}$. With $2\hbar\omega_0 < 2|\mu| < 3\hbar\omega_0$, the value of $|\chi^{(3)}_{xxxx}|$ increases further as both one-photon and two-photon resonant transitions are blocked with $G\left(\frac{\hbar\omega_0}{2|\mu|}\right) \sim 0$ and $G\left(\frac{2\hbar\omega_0}{2|\mu|}\right) \sim 0$. Finally, for $2|\mu| > 3\hbar\omega_0$, all resonant transitions are blocked, leaving again a vanishingly small $\chi^{(3)}_{xxxx}$ from nonresonant contributions. The calculated μ-dependence of $\chi^{(3)}_{xxxx}$ with $\hbar\omega_0 = 0.956$ eV is plotted in Fig. 4b.

While the analytic expression captures the essence of the THG response, the detailed shape of the curve is far from reality because resonant damping and finite electron temperature effects have been neglected. For better comparison with experiment, we include the finite electron temperature (T_e) effect on $\Delta n(\mu)$ and proper resonant damping factors ($\Gamma_e = 0.2 \times |\mu|$ eV (ref. [39]) and $\Gamma_i = 0.5$ meV (ref. [29]) for interband and intraband resonances, respectively) in the calculation (Fig. 4c). Both have the effect of smearing out the sharp features, making the calculated spectrum comparable with experiment. As described in detail in the Supplementary Information, the quasi-equilibrium electron temperature T_e can be very high if interband excitations of electrons is strong[40,41]. This happens when the one-photon transition is allowed ($2|\mu| < \hbar\omega_0$); for an incident fluence of 3.14 J m^{-2} from a 200 fs pulse, T_e reaches about 2,100 K. However, if the one-photon transition is blocked ($2|\mu| > \hbar\omega_0$), the electron temperature rise is negligible, and T_e remains essentially at the room temperature (300 K). The temperature effect on THG actually is not very significant because $|\chi^{(3)}_{xxxx}|$ is small in the range of $2|\mu| < \hbar\omega_0$ (Supplementary Fig. 1).

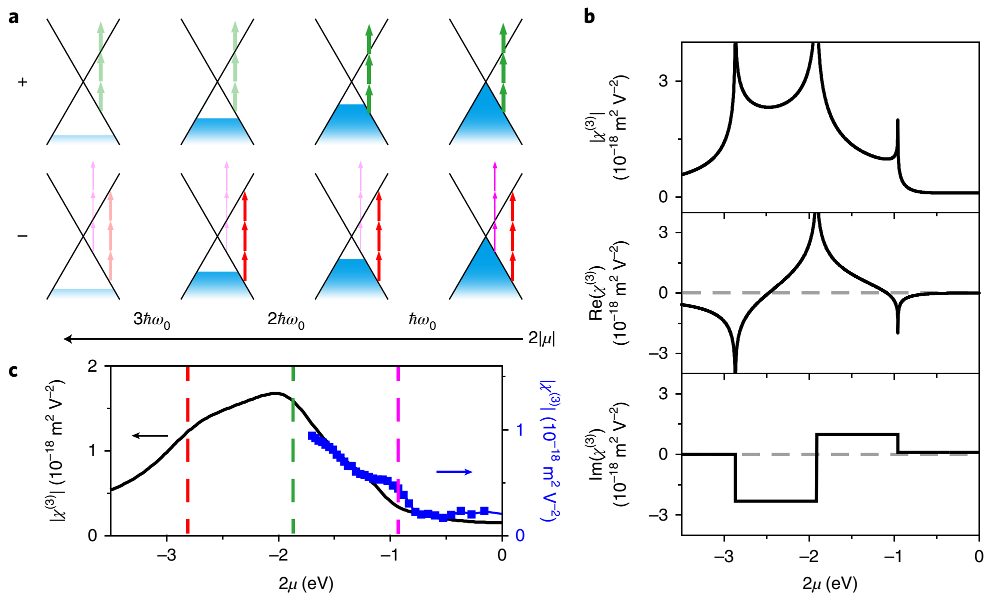

Fig. 4 | Theoretical understanding of μ-dependent $\chi^{(3)}$ in THG. a, Schematics showing how increase of $|\mu|$ successively switches off one-photon (magenta), two-photon (green) and three-photon (red) interband transitions by Pauli blocking in graphene. The switch-off is gradual at finite temperature and damping and is described by the reduced brightness of the arrows. Two-photon transition contributes to $\chi^{(3)}_{xxxx}$ positively, while one- and three-photon transitions contribute negatively. **b**, Calculated $\chi^{(3)}_{xxxx}$ versus μ for THG at $3\hbar\omega_0 = 2.868$ eV from graphene at zero temperature with resonant damping neglected, exhibiting singularities at $|2\mu| = \hbar\omega_0$, $2\hbar\omega_0$ and $3\hbar\omega_0$. **c**, Comparison between experimental data (blue squares) and theoretical simulation (black curve) taking into account the finite temperature and resonant damping effects. $T_e = 300$ K and 2,100 K for $|2\mu| > \hbar\omega_0$ and $\mu = 0$, respectively, $\Gamma_e = 0.2 \times |\mu|$ eV and $\Gamma_i = 0.5$ meV. The dashed lines mark the positions of $|2\mu| = \hbar\omega_0$ (magenta), $2\hbar\omega_0$ (green) and $3\hbar\omega_0$ (red).

Similar discussion can be applied to FWM. The third-order susceptibility $\chi^{(3)}_{xxxx}$ for the two-colour SFM ($2\omega_1+\omega_2$ and $\omega_1+2\omega_2$) increases with $|\mu|$ as for THG, but there are five resonant transitions for each SFM process, including: the one-photon transitions at $\hbar\omega_1$ and $\hbar\omega_2$, two-photon transitions at $2\hbar\omega_1$ (or $2\hbar\omega_2$) and $\hbar(\omega_1+\omega_2)$, and three-photon transition at $\hbar(2\omega_1+\omega_2)$ (or $\hbar(\omega_1+2\omega_2)$). Figure 5a shows the calculated $\chi^{(3)}_{xxxx}$ versus μ for $\omega_1+2\omega_2$ SFM at zero temperature and without resonant damping. The characteristic features around the five specific values of μ are clearly seen. The expression of $\chi^{(3)}_{xxxx}$ for SFM is given by Supplementary equation (3-4). Again, the terms for two-photon transitions have opposite sign with respect to the terms for one- and three-photon transitions, leading to a much weaker $|\chi^{(3)}_{xxxx}|$ when $2|\mu| < \hbar\omega_1$ and $\hbar\omega_2$. Given the finite electron temperature and resonant damping effects, resonances due to one-photon and two-photon transitions are greatly smeared, as shown in Fig. 5b. Similar to the THG case, the effect of high T_e for $2|\mu| < \hbar\omega_1$ (assuming $\omega_1 > \omega_2$) is not very significant in SFM. The theoretical simulation reasonably agrees with the experimental result plotted in Fig. 5b.

In sharp contrast to SFM, the DFM processes ($2\omega_1-\omega_2$ and $2\omega_2-\omega_1$) show opposite μ-dependence with the output strongest at $\mu \sim 0$. The expression of $\chi^{(3)}_{xxxx}$ for DFM is the same as that for SFM except for a flip of sign on ω_1 or ω_2 (see the Supplementary Information). Pauli blocking occurs at $2|\mu| > \hbar\omega_1$ and $\hbar\omega_2$ for one-photon transitions, $2|\mu| > 2\hbar\omega_1$ (or $2\hbar\omega_2$) and $\hbar(\omega_1-\omega_2)$ for two-photon transitions, and $2|\mu| > \hbar(2\omega_1-\omega_2)$ (or $\hbar(2\omega_2-\omega_1)$) for three-photon transition. The corresponding characteristic features can again be seen in the calculated $\chi^{(3)}_{xxxx}$ versus μ (Fig. 5c for the $2\omega_1-\omega_2$ DFM process). Note that the feature at $2|\mu| = \hbar|\omega_1-\omega_2|$ is present, but is very weak and hardly visible in Fig. 5c, because it is described by a $G\left(\frac{\hbar\,|\,\omega_1-\omega_2\,|}{2\,|\,\mu\,|}\right)$ term with a coefficient proportional to $(\omega_1-\omega_2)^3$. Increase or decrease at each step of the change depends on the sign of the frequency factor associated with each type of transition. It is seen that for the $2\omega_1-\omega_2$ DFM process, there are three terms in the equation for $\chi^{(3)}_{xxxx}$ that have the frequency factor $(\omega_1-\omega_2)^2$ in the denominator. They contribute dominantly to $\chi^{(3)}_{xxxx}$ when $2|\mu| < \hbar\omega_2$, especially if ω_2 is close to ω_1, and yield a large step change when each term drops off at a specific value of $|\mu|$ because of Pauli blocking of the specific type of resonant transitions. The exceptionally large $\chi^{(3)}_{xxxx}$ for DFM is in strong contrast to the very weak $\chi^{(3)}_{xxxx}$ for SFM. Inclusion of the finite electron temperature and resonant damping effects in the calculation of $\chi^{(3)}_{xxxx}$ as a function of μ again smears out the peaks and spreads out the curve. In this case, the effect of high T_e for $2|\mu| < \hbar\omega_1$ (assuming $\omega_1 > \omega_2$) is more significant; as $|\mu|$ decreases towards zero, it causes $|\chi^{(3)}_{xxxx}|$ to increase less and spread out more (Supplementary Fig. 2). The calculated curve of $|\chi^{(3)}_{xxxx}|$ versus μ agrees fairly well with the experimental results, as shown in Fig. 5d and Supplementary Fig. 2.

We note that as long as $2|\mu| < \hbar\omega_1$ or $\hbar\omega_2$, the $2\omega_1-\omega_2$ and $2\omega_2-\omega_1$ DFM would appear divergent through the frequency factor $(\omega_1-\omega_2)^{-2}$ as ω_1 approaches ω_2 (Supplementary equation (3-6) or (3-7)). One therefore expects that degenerate FWM including self-phase modulation would be extraordinarily strong in undoped graphene ($\mu = 0$). This was not noticed in the early pioneering work of Hendry et al.[16]. To experimentally verify such a behaviour, we measured DFM of $2\omega_1-\omega_2$ with μ close to zero, ω_1 fixed at 1.195 eV (1,040 nm), and ω_2 tuned from 0.956 eV (1,300 nm) to 1.11 eV (1,120 nm). As shown in Fig. 5e, $\chi^{(3)}_{xxxx}$ for DFM increased by approximately three times as $\Delta\omega = \omega_1 - \omega_2$ decreased and agrees fairly well with the theoretical calculation. We expect a more rapid rise of DFM if DFM at smaller $\Delta\omega$ could be measured.

We adopted the scheme of ref. [12] to measure the average output power of THG and FWM and estimated the value of $|\chi^{(3)}_{xxxx}|$ for the processes (see the Supplementary Information). We found for THG at $\hbar\omega_0 = 0.956$ eV and $2|\mu| < \hbar\omega_0$, $|\chi^{(3)}_{xxxx}| = 1.9 \pm 0.3 \times 10^{-19}$ m^2 V^{-2}. This value is very close to the theoretical value of $|\chi^{(3)}_{xxxx}| = 1.0 \times 10^{-19}$ m^2 V^{-2}. In comparison, our value is about two to three orders of magnitude smaller than that of Kumar et al.[12], but consistent with the recent work of Woodward et al.[15], assuming $2|\mu| < \hbar\omega_0$

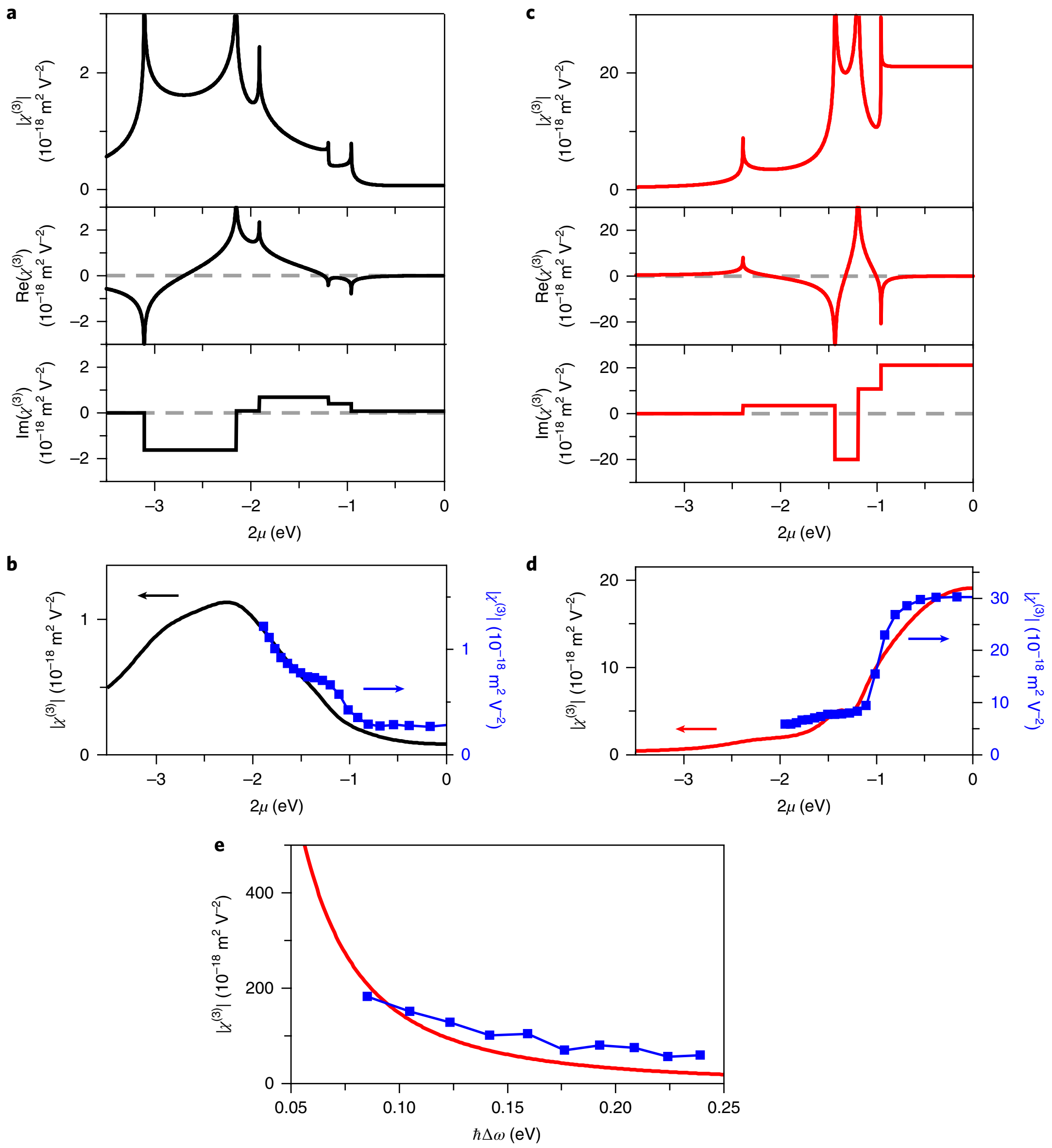

Fig. 5 | Theoretical calculations of μ-dependent $\chi^{(3)}$ and comparison with experimental data for FWM from graphene. a,b, Calculated $\chi^{(3)}_{xxxx}$ for $\omega_1+2\omega_2$ SFM at $T=0$ K with no resonant damping (**a**) and at finite temperature with damping (**b**). **c**,**d**, Calculated $\chi^{(3)}_{xxxx}$ for $2\omega_1-\omega_2$ DFM at $T=0$ K with no resonant damping (**c**) and at finite temperature with damping (**d**). $\hbar\omega_1=1.195$ eV and $\hbar\omega_2=0.956$ eV. Corresponding experimental data (blue squares) are presented in **b** and **d** for comparison. The electron temperatures used in the calculation are $T_e=300$ K for $|2\mu|>\hbar\omega_1$ and T_e=1,550 K and 1,750 K for $\mu=0$, respectively. The damping parameters are the same as those in Fig. 4c. **e**, Calculated $|\chi^{(3)}_{xxxx}|$ for DFM at $2\omega_1-\omega_2$ from undoped graphene ($\mu=0$) as a function of $\Delta\omega$ ($=\omega_1-\omega_2$) at $T=0$ K with no damping showing divergence towards $\Delta\omega=0$. Blue squares are experimental data with ω_1 fixed at 1,040 nm and ω_2 tuned from 1,120 nm to 1,300 nm, with incident fluences of 1.0 J m^{-2} and 0.95–1.33 J m^{-2}, respectively.

was satisfied in their experiments. For DFM, our experimental value of $|\chi^{(3)}_{xxxx}|$ is also close to the theoretical one as seen in Fig. 5e. It is seen that the measured values of $|\chi^{(3)}_{xxxx}|$ for THG and FWM in undoped graphene varies by about three orders of magnitude, and it could be further enhanced by another few orders if FWM moves towards degeneracy.

Conclusions

We have demonstrated that the third-order nonlinearity of graphene is exceptionally large and can be varied by orders of magnitude with the help of gate-controlled doping or shift of the chemical potential. The results can be understood from a unified theory on FWM in graphene. It is now possible to well predict the dependence of the third-order nonlinear responses of graphene on input frequencies and doping level. The understanding can be extended to other nonlinear optical processes in graphene, such as effective second-order processes[42–44], and even high-order harmonic generation[25]. In general, the optical nonlinearity of linear-band materials with the chemical potential close to the Dirac or Weyl point tends to diverge in cases where input frequency combination approaches zero. The resulting giant nonlinearity of such materials, particularly graphene, can be of great use in future optoelectronic devices[6].

Methods

Methods, including statements of data availability and any associated accession codes and references, are available at https://doi.org/10.1038/s41566-018-0175-7.

Received: 14 August 2017; Accepted: 19 April 2018;

References

1. Bonaccorso, F., Sun, Z., Hasan, T. & Ferrari, A. C. Graphene photonics and optoelectronics. *Nat. Photon.* **4**, 611–622 (2010).
2. Koppens, F. H. L., Chang, D. E. & García de Abajo, F. J. Graphene plasmonics: a platform for strong light-matter interactions. *Nano Lett.* **11**, 3370–3377 (2011).
3. Nair, R. R. et al. Fine structure constant defines visual transparency of graphene. *Science* **320**, 1308–1308 (2008).
4. Mak, K. F. et al. Measurement of the optical conductivity of graphene. *Phys. Rev. Lett.* **101**, 196405 (2008).
5. Koppens, F. H. L. et al. Photodetectors based on graphene, other two-dimensional materials and hybrid systems. *Nat. Nanotech.* **9**, 780–793 (2014).
6. Sun, Z., Martinez, A. & Wang, F. Optical modulators with 2D layered materials. *Nat. Photon.* **10**, 227–238 (2016).
7. Wang, F. et al. Gate-variable optical transitions in graphene. *Science* **320**, 206–209 (2008).
8. Liu, M. et al. A graphene-based broadband optical modulator. *Nature* **474**, 64–67 (2011).
9. Chen, C. et al. Controlling inelastic light scattering quantum pathways in graphene. *Nature* **471**, 617–620 (2011).
10. Mikhailov, S. A. Non-linear electromagnetic response of graphene. *Europhys. Lett.* **79**, 27002 (2007).
11. Glazov, M. M. & Ganichev, S. D. High frequency electric field induced nonlinear effects in graphene. *Phys. Rep.* **535**, 101–138 (2014).
12. Kumar, N. et al. Third harmonic generation in graphene and few-layer graphite films. *Phys. Rev. B* **87**, 121406 (2013).
13. Hong, S. et al. Optical third-harmonic generation in graphene. *Phys. Rev. X* **3**, 021014 (2013).
14. Säynätjoki, A. et al. Rapid large-area multiphoton microscopy for characterization of graphene. *ACS Nano* **7**, 8441–8446 (2013).
15. Woodward, R. I. et al. Characterization of the second- and third-order nonlinear optical susceptibilities of monolayer MoS_2 using multiphoton microscopy. *2D Mater.* **4**, 011006 (2017).
16. Hendry, E., Hale, P. J., Moger, J., Savchenko, A. K. & Mikhailov, S. A. Coherent nonlinear optical response of graphene. *Phys. Rev. Lett.* **105**, 097401 (2010).
17. Ciesielski, R. et al. Graphene near-degenerate four-wave mixing for phase characterization of broadband pulses in ultrafast microscopy. *Nano Lett.* **15**, 4968–4972 (2015).
18. Zhang, H. et al. Z-scan measurement of the nonlinear refractive index of graphene. *Opt. Lett.* **37**, 1856–1858 (2012).
19. Yang, H. et al. Giant two-photon absorption in bilayer graphene. *Nano Lett.* **11**, 2622–2627 (2011).
20. Dremetsika, E. et al. Measuring the nonlinear refractive index of graphene using the optical Kerr effect method. *Opt. Lett.* **41**, 3281–3284 (2016).
21. Vermeulen, N. et al. Negative Kerr nonlinearity of graphene as seen via chirped-pulse-pumped self-phase modulation. *Phys. Rev. Appl.* **6**, 044006 (2016).
22. Gu, T. et al. Regenerative oscillation and four-wave mixing in graphene optoelectronics. *Nat. Photon.* **6**, 554–559 (2012).
23. Wu, R. et al. Purely coherent nonlinear optical response in solution dispersions of graphene sheets. *Nano Lett.* **11**, 5159–5164 (2011).
24. Sun, D. et al. Coherent control of ballistic photocurrents in multilayer epitaxial graphene using quantum interference. *Nano Lett.* **10**, 1293–1296 (2010).
25. Yoshikawa, N., Tamaya, T. & Tanaka, K. High-harmonic generation in graphene enhanced by elliptically polarized light excitation. *Science* **356**, 736–738 (2017).
26. Giorgianni, F. et al. Strong nonlinear terahertz response induced by Dirac surface states in Bi_2Se_3 topological insulator. *Nat. Commun.* **7**, 11421 (2016).
27. Wu, L. et al. Giant anisotropic nonlinear optical response in transition metal monopnictide Weyl semimetals. *Nat. Phys.* **13**, 350–355 (2016).
28. Cheng, J. L., Vermeulen, N. & Sipe, J. E. Third order optical nonlinearity of graphene. *New J. Phys.* **16**, 53014 (2014).
29. Cheng, J. L., Vermeulen, N. & Sipe, J. E. Third-order nonlinearity of graphene: effects of phenomenological relaxation and finite temperature. *Phys. Rev. B* **91**, 235320 (2015).
30. Margulis, V. A., Muryumin, E. E. & Gaiduk, E. A. Frequency dependence of optical third-harmonic generation from doped graphene. *Phys. Lett. A* **380**, 304–310 (2016).
31. Mikhailov, S. A. Quantum theory of the third-order nonlinear electrodynamic effects of graphene. *Phys. Rev. B* **93**, 085403 (2016).
32. Rostami, H. & Polini, M. Theory of third-harmonic generation in graphene: a diagrammatic approach. *Phys. Rev. B* **93**, 161411 (2016).
33. Das, A. et al. Monitoring dopants by Raman scattering in an electrochemically top-gated graphene transistor. *Nat. Nanotech.* **3**, 210–215 (2008).
34. Ye, J. T. et al. Liquid-gated interface superconductivity on an atomically flat film. *Nat. Mater.* **9**, 125–128 (2009).
35. Li, Z. Q. et al. Dirac charge dynamics in graphene by infrared spectroscopy. *Nat. Phys.* **4**, 532–535 (2008).
36. Liu, W. T. et al. Nonlinear broadband photoluminescence of graphene induced by femtosecond laser irradiation. *Phys. Rev. B* **82**, 081408 (2010).
37. Shen, Y. R. *The Principles of Nonlinear Optics* (Wiley-Interscience, New York, NY, 1984).
38. Boyd, R. W. *Nonlinear Optics* (Academic Press, New York, NY, 2008).
39. Sarma, S. D., Adam, S., Hwang, E. H. & Rossi, E. Electronic transport in two-dimensional graphene. *Rev. Mod. Phys.* **83**, 407–470 (2011).
40. Lui, C. H., Mak, K. F., Shan, J. & Heinz, T. F. Ultrafast photoluminescence from graphene. *Phys. Rev. Lett.* **105**, 127404 (2010).
41. Shi, S.-F. et al. Controlling graphene ultrafast hot carrier response from metal-like to semiconductor-like by electrostatic gating. *Nano Lett.* **14**, 1578–1582 (2014).
42. Constant, T. J., Hornett, S. M., Chang, D. E. & Hendry, E. All-optical generation of surface plasmons in graphene. *Nat. Phys.* **12**, 124–127 (2015).
43. Cheng, J. L., Vermeulen, N. & Sipe, J. E. Second order optical nonlinearity of graphene due to electric quadrupole and magnetic dipole effects. *Sci. Rep.* **7**, 43843 (2017).
44. Wang, Y., Tokman, M. & Belyanin, A. Second-order nonlinear optical response of graphene. *Phys. Rev. B* **94**, 195442 (2016).

Acknowledgements

The work at Fudan University was supported by the National Basic Research Program of China (grant no. 2014CB921601), National Key Research and Development Program of China (grant nos. 2016YFA0301002, 2016YFA0300900), National Natural Science Foundation of China (grant no. 91421108, 11622429, 11374065), and the Science and Technology Commission of Shanghai Municipality (grant no. 16JC1400401). Part of the sample fabrication was performed at Fudan Nano-fabrication Laboratory. K.L. is supported by the National Natural Science Foundation of China (grant no. 51522201). J.E.S. is supported by the Natural Sciences and Engineering Research Council of Canada. Y.-R.S. acknowledges support from the Director, Office of Science, Office of Basic Energy Sciences, Materials Sciences and Engineering Division, US Department of Energy (contract no. DE-AC03-76SF00098).

Author contributions

S.W. and W.-T.L. conceived and supervised the project. T.J., D.H., Y.S. and Y.Y. prepared the devices and performed the experiments, with assistance from Y.D., L.S. and J.Z. on gate-dependent optical transmittance measurement. X.F., Z.Z., K.L. and C.Z. provided the chemical vapour deposition-grown graphene samples. T.J., D.H., J.C., J.E.S., Y.-R.S., W.-T.L. and S.W. analysed the data. T.J., D.H., J.E.S., Y.-R.S., W.-T.L. and S.W. wrote the paper with contributions from all authors.

Competing interests

The authors declare no competing interests.

Additional information

Supplementary information is available for this paper at https://doi.org/10.1038/s41566-018-0175-7.

Reprints and permissions information is available at www.nature.com/reprints.

Correspondence and requests for materials should be addressed to W.-T.L. or S.W.

Methods

Device fabrication. Single crystalline[45,46] or polycrystalline[47] graphene monolayers used in the experiment were grown by chemical vapour deposition and transferred onto fused silica substrates. Source, drain and gate electrodes (50 nm Au and 5 nm Cr) were patterned through a dry stencil mask by electron beam deposition. All the electrodes were wire-bonded to a chip carrier for electrical control. Ion-gel gating was achieved by uniformly applying freshly prepared ion-gel solution onto the graphene devices, and further drying in a glove box filled with high-purity argon gas. The ion-gel solution was prepared by dissolving 16.7 mg of poly(styrene-*b*-ethylene oxide-*b*-styrene) (PS-PEO-PS) and 0.5 g of 1-ethyl-3-methylimidazolium bis(trifluoromethylsulfonyl)imide ([EMIM][TFSI]) into 1.82 ml of dry dichloromethane. PS-PEO-PS, [EMIM][TFSI] and dry dichloromethane were purchased from J&K Scientific. Experimental results of THG and FWM from single crystalline and polycrystalline graphene, as well as exfoliated monolayer, were found to be very much the same.

Characterization and measurement. The device characterization and experimental measurement were conducted in sample scanning optical microscopes that combined with femtosecond laser systems and an electrical transport setup. During the whole measurement, the graphene device was maintained in a dry nitrogen environment at room temperature. The CNP of graphene was determined by its maximum resistance in response to V_g as shown in Fig. 1b. A Fourier transform infrared spectrometer (VERTEX 70) was used to measure the transmittance spectra of gated graphene, from which μ was deduced as described in the main text and in the Supplementary Information.

For THG measurements, a linearly polarized femtosecond laser beam (MaiTai HP and Inspire Auto, Spectra Physics) tunable from 345 to 2,500 nm was focused and normally incident on graphene through a microscopic objective (100×, numerical aperture 0.95, Nikon), and the reflected THG signal was collected. The sample sitting on a nano-positioning stage enabled us to locate defect-free areas on the sample. A single-photon counting silicon avalanche photodetector (Perkin-Elmer) or a fibre-coupled spectrograph equipped with a liquid-nitrogen-cooled silicon charge-coupled device (Princeton Instruments) was used to detect the THG signal after proper filtering. The detailed optical arrangement is depicted in Supplementary Fig. 3a. For measurement of the polarization-dependent azimuthal pattern of THG measurement (displayed in Fig. 2d,e), the transmitted THG geometry was adopted with the setup sketched in Supplementary Fig. 3b.

For FWM measurements, a different femtosecond laser system (Insight Deepsee, Spectra Physics) was used, which could simultaneously produce two beams of different wavelengths at a repetition rate of 80 MHz, one tunable from 700 to 1,300 nm and the other fixed at 1,040 nm. The two beams were sent collinearly on the sample at normal incidence through a scanning optical microscope and the reflected FWM signal was detected. For the DFM signals in Fig. 3d,f (blue dots), the spectra were recorded by a fibre-coupled spectrograph equipped with a liquid-nitrogen-cooled InGaAs array detector (PyLoN-IR, Princeton Instruments).

Data availability. The data that support the plots within this paper and other findings of this study are available from the corresponding authors upon reasonable request.

References

45. Xu, X. Z. et al. Ultrafast growth of single-crystal graphene assisted by a continuous oxygen supply. *Nat. Nanotech.* **11**, 930–935 (2016).
46. Xu, X. Z. et al. Ultrafast epitaxial growth of metre-sized single-crystal graphene on industrial Cu foil. *Sci. Bull.* **62**, 1074–1080 (2017).
47. Li, X. et al. Large-area synthesis of high-quality and uniform graphene films on copper foils. *Science* **324**, 1312–1314 (2009).